RSC Advances

PAPER

View Article Online
View Journal | View Issue

Cite this: *RSC Adv.*, 2024, **14**, 3952

Aluminum-based ceramic/metal composites with tailored thermal expansion fabricated by spark plasma sintering

Hui Wei, *[a] Chuan Li,[b] Yan Xu,[c] Xu Zhang,[c] Jing Li, [a] Yang Han,[a] Mingling Li[a] and Xiaoyong Xu*[a]

We have devised a moderate temperature spark plasma sintering route for preparing aluminum matrix composites which possess tailored coefficients of thermal expansion (CTEs) in combination with tunable electrical and thermal conductivities. Due to its isotropic negative thermal expansion over a wide temperature range, cubic-phase $ZrW_{2-x}Mo_xO_8$ ($x = 0.0$, 1.0) is an ideal secondary phase for metal matrix composites with suitable CTEs. In this study, high-density ZrW_2O_8/Al and $ZrWMoO_8$/Al composites containing 30–70 vol% Al were fabricated using spark plasma sintering. X-ray diffraction analysis indicated that the composites were composed of a thermally-stable cubic phase at temperatures as high as 873 K for ZrW_2O_8 and 773 K for $ZrWMoO_8$, without any orthorhombic high-pressure phase derived from the large thermal mismatch between the ceramic and metal during sintering. The thermal expansion curves of the $ZrW_{2-x}Mo_xO_8$/Al composites were consistent with the predictions made using the Rule-of-Mixtures. The CTEs could be controlled from negative to positive and even close to zero by simply varying the volume fraction of aluminum. Similarly, the thermal and electrical conductivity of the $ZrW_{2-x}Mo_xO_8$/Al composites increases with increasing Al content, which is thought to be mainly related to the contribution of the free electron conduction path of Al in the composites.

Received 7th November 2023
Accepted 20th January 2024

DOI: 10.1039/d3ra07593a

rsc.li/rsc-advances

1. Introduction

Aluminum matrix composites are widely used for industrial production because of aluminum's low density, easy processability, and good heat and electrical conductivity at room temperature and normal pressure. Another important aspect is that aluminum has a relatively high coefficient of thermal expansion of 23.21×10^{-6} K^{-1}, which is significant compared to other metals or alloy materials (copper: 16.6×10^{-6} K^{-1}, steel: 11.5×10^{-6} K^{-1}, titanium: 8.2×10^{-6} K^{-1}, silver: 18.9×10^{-6} K^{-1}). When Aluminum is used in combination with a thermal expansion inhibiting material, the property of having a large coefficient of thermal expansion allows for a wider adjustment of the desired coefficient of thermal expansion. At the same time, it preserves the excellent electrical and thermal conductivity of Al as much as possible. This flexibility improves the applicability of aluminum matrix composites in a variety of situations. It is, thus, anticipated that the addition of a material with a negative thermal expansion (NTE) to an aluminum matrix can help achieve precisely-matched thermal expansion (positive, negative, or even zero) by adjusting the volume fractions of the different phases in such composites. These composites have potentially useful applications in heat sinks, thermoelectric modules, and other electronic devices.[1–3]

Cubic-phase ZrW_2O_8 is a typical material with a negative thermal expansion, which demonstrates a large three-dimensional isotropic NTE coefficient (-8.8 to -4.9×10^{-6} K^{-1}) over a wide temperature range (0.3–1050 K).[4–7] These characteristics render it an ideal secondary phase for aluminum matrix composites with suitable thermal expansion coefficients. Near 443 K, ZrW_2O_8 undergoes a reversible order–disorder phase transition from a low-temperature acentric cubic phase (α-ZrW_2O_8: -8.8×10^{-6} K^{-1}) to a high-temperature centric cubic phase (β-ZrW_2O_8: -4.9×10^{-6} K^{-1}).[6–8] The abrupt change of NTE coefficient is a disadvantage in practical applications if the phase transition temperature of the materials is within the working temperature range. Numerous investigations have confirmed that the phase transition temperature of ZrW_2O_8 can be adjusted through Mo^{6+} partially doping in W^{6+}, which it was reported that increasing the Mo content in $ZrW_{2-x}Mo_xO_8$ leads to a lower phase transition temperature.[9–13] J. S. O. Evans *et al.*[10] reported that the α–β phase transition temperature shifted to below room temperature for $ZrWMoO_8$ by conducting neutron powder diffraction experiments, indicating that $ZrWMoO_8$ is also a very promising inhibitor of thermal expansion. However, due to its relatively modest thermal expansion coefficient above

[a]*Engineering Research Center of High-frequency Soft Magnetic Materials and Ceramic Powder Materials of Anhui Province, Chaohu University, 1 Bantang Road Chaohu, Hefei, 238024, P. R. China. E-mail: little_weihui@yahoo.co.jp; 053063@chu.edu.cn*
[b]*Baoji Oilfield Machinery Co., Ltd, Baoji, 721002, P. R. China*
[c]*Hefei Jingchuang Technology Co., Ltd, Hefei, 231500, P. R. China*

room temperature (-3.5×10^{-6} K^{-1}), its applicability to composite materials is somewhat limited. Therefore, comparing the thermal expansion properties of composites by incorporating ZrW_2O_8 and $ZrWMoO_8$ separately as thermal expansion inhibitors with Al is crucial for practical applications.

In addition, low-temperature cubic phase α-ZrW_2O_8 transforms into an orthorhombic phase (γ-ZrW_2O_8), when subjected to pressures above 0.2 GPa, with a dramatically low NTE coefficient, which decreases from -8.8 to -1.0×10^{-6} K^{-1}.[14–16] It has been reported that γ-ZrW_2O_8 was formed during ZrW_2O_8/Al composite sintering, wherein the cubic–orthorhombic phase transition strongly influenced the thermal properties of the composites, due to the different thermal expansion coefficients of the ceramic and metal matrix particles.[1,17,18] Similar phenomena were also observed in other metal matrix composites containing ZrW_2O_8 particles such as ZrW_2O_8/Cu, ZrW_2O_8/Al–Si composites.[19–24] The biggest disadvantage of ZrW_2O_8/Al composites is their high sintering temperature, which causes ZrW_2O_8 to decompose into ZrO_2 and WO_3 above 1050 K, whereas the melting point of aluminum is about 933 K.[25] Therefore, a low-temperature, low-pressure sintering method is needed for the fabrication of $ZrW_{2-x}Mo_xO_8$/Al composites in order to suppress the α–γ phase transition.

Spark plasma sintering (SPS) is a promising method for bonding various kinds of solid materials (*e.g.*, metal to metal, metal-to-ceramic, *etc.*). The mechanism of SPS involves the instantaneous generation of high-temperature spark plasma in the gap due to the discharge effect between the powder particles. Throughout the SPS process, the combined effects of spark discharge (leading to the generation of spark plasma and localized spark impact pressure), Joule heating, electrodiffusion, and plastic deformation contribute to fast and efficient sintering. Our group synthesized single-phase ZrW_2O_8 ceramics and ZrW_2O_8/SiO_2 and ZrW_2O_8/Cu composites at 873 K and 50 MPa by using SPS.[26,27] Since the melting point of aluminum is about 933 K, this coincides well with the synthesis temperature of ZrW_2O_8 in our past work, which facilitates a better synergy between the two materials in the composite process. In this study, dense $ZrW_{2-x}Mo_xO_8$/Al ($x = 0.0$, 1.0) composites containing 30 to 70 vol% Al were fabricated using SPS. We investigated the effects of $ZrW_{2-x}Mo_xO_8$ as thermal expansion inhibitors on the thermal expansion properties of the composites and carried out a comparison of the thermal expansion curves with predictions made using the Rule-of-Mixtures. In addition, the thermal conductivity and electrical conductivity of the $ZrW_{2-x}Mo_xO_8$/Al composites were evaluated to explore the application prospects of the composites.

2. Experimental

2.1 Fabrication of $ZrW_{2-x}Mo_xO_8$/Al ($x = 0.0$, 1.0) composites

ZrW_2O_8/Al composites and $ZrWMoO_8$/Al composites were fabricated by spark plasma sintering method. High-purity cubic-phase ZrW_2O_8 and $ZrWMoO_8$ powders were synthesized using a sol–gel-hydrothermal method.[28] First, $ZrOCl_2 \cdot 8H_2O$ (Kishida Chemical, Japan, 99%) was dissolved in 4 mol L^{-1} acetic acid and 2-butanol in the air for 3 hours. At the same time, WCl_6 (High Purity Chemicals, Japan, 99.99%), $MoCl_5$ (Sigma-Aldrich, USA, 95%), were separately dissolved in ethanol under Nitrogen atmosphere. After stirring for 3 hours, the tungsten and molybdenum solutions were poured into zirconium solution for 72 hours stirring. Subsequently, the mixed solution of tungsten, molybdenum and zirconium was heated in a silicone oil bath at around 360 K. The sol–gel precursors were obtained after the solution had been completely evaporated.

The second stage is referred to as the hydrothermal stage. The obtained sol–gel precursors were dissolved in 60 mL of distilled water and after addition to a 100 mL Teflon-lined Parr bomb, placed in a mantle heater at 453 K for 18 hours with continuous stirring. The sol–gel-hydrothermal precursors were finally centrifuged, washed with distilled H_2O, and dried in an oven at 333 K. The sol–gel-hydrothermal precursors were precalcined at 873 K for ZrW_2O_8 in a drying oven (DX-41, Yamato Scientific, Tokyo, Japan). Aluminum powders (Kojundo Chemical, 99.99%, Tokyo, Japan) were mixed with ZrW_2O_8 and $ZrWMoO_8$ powders at various volume ratios (0 vol% Al, 30 vol% Al, 50 vol% Al, 70 vol% Al, 100 vol% Al). Ethanol was added to the mixed powders, and the mixture was kneaded for 30 min in an agate mortar. After kneading, the mixed powders were placed in a drying oven at 373 K for 3 h. The mixed powders were filled in graphite dies (10 mm in diameter and 20 mm in depth) separately and wrapped in carbon sheets. An SPS apparatus (SPS-515S; Fuji Electronic Industrial, Saitama, Japan), with a pulse duration of 3.3 ms and on/off pulse intervals of 12 : 2, was used to fabricate dense ZrW_2O_8/Al and $ZrWMoO_8$/Al composites. The composites were sintered at 873 K (ZrW_2O_8/Al) and 773 K ($ZrWMoO_8$/Al) for 10 min at a heating rate of 100 K min^{-1} to obtain $ZrW_{2-x}Mo_xO_8$/Al composites. During SPS, the applied pressure was held constant at 90 MPa in an argon atmosphere, until the conclusion of the sintering process. The volume contraction between the two graphite punches, namely the *Z*-axis linear shrinkage value, was recorded every 30 s during SPS. The *Z*-axis linear shrinkage curve of Al 50 vol% ZrW_2O_8/Al composite and optical photos of ZrW_2O_8/Al composites with different Al volume fractions are shown in Fig. 1.

2.2 Evaluation methods

Phase identification of $ZrW_{2-x}Mo_xO_8$/Al ($x = 0.0$, 1.0) composites was carried out using powder X-ray diffraction (Rigaku, Ultima IV, Tokyo, Japan). XRD data were collected at a scan speed of 6° min^{-1}, with the 2θ ranging from 10° to 80° under 40 kV/40 mA using Cu-Kα radiation ($\lambda = 0.15406$ nm) employing the continuum scanning method. The morphological composition of the samples was systematically evaluated using a field-emission scanning electron microscope (HITACHI, SU8230, Tokyo, Japan) equipped with an energy-dispersive X-ray (EDX) spectrometer. The applied voltage included an accelerating voltage of 3.0 kV, and the current parameters were set to an electron beam current of 10 100 nA. The coefficients of thermal expansion of the samples were measured with a thermodynamic analyzer (Shimadzu, TMA-60/60H, Kyoto, Japan). The data were collected at a heating rate of 1 K min^{-1} from 323 to

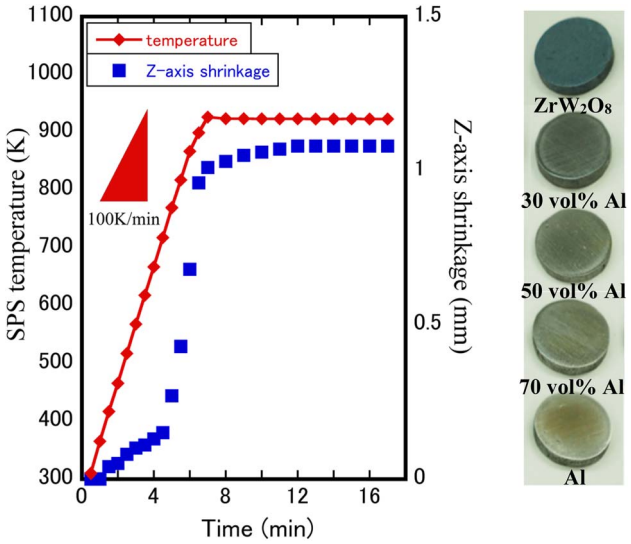

Fig. 1 *Z*-axis linear shrinkage curve of Al 50 vol% ZrW_2O_8/Al composite and optical photos of ZrW_2O_8/Al composites.

523 K and three replicate experiments were carried out. The theoretical CTEs of the composites were calculated using the Rule-of-Mixtures. The Rule of Mixtures (ROM) is a theoretical framework used to predict the properties of composite materials based on the volume fractions and properties of the individual components. ROM considers the matrix to be free of voids, in which each material is perfectly bonding to the matrix so that each component is distorted independently. Coefficients of thermal expansion are usually assumed to follow a linear ROM dependence on the volume fraction. The CTE values used were as follows: 23×10^{-6} K^{-1} for Al, -8.8×10^{-6} K^{-1} for low-temperature cubic phase α-ZrW_2O_8, -4.9×10^{-6} K^{-1} for high-temperature cubic phase β-ZrW_2O_8, and -3.5×10^{-6} K^{-1} for $ZrWMoO_8$.[29] The relative densities of the composites were measured by Archimedes' principle using distilled water. The specific Archimedes method steps are as follows: obtain post-sintered samples of ZrW_2O_8/Al and $ZrWMoO_8$/Al composite materials, ensuring that their surfaces are clean and free of impurities. Then, use a precision balance to weigh the mass of each sample and record the accurate mass values (m_1). Subsequently, gently and uniformly immerse the samples in deionized water, ensuring that no bubbles adhere to the sample surfaces. Wait for stability and record the mass of the samples when submerged in deionized water (m_2). Calculate the relative density (ρ_r) using the following formula: $\rho_r = m_1/[(m_1 - m_2) \times \rho_l]$, where ρ_l is the density of deionized water at ambient temperature. The measured density of all specimens as well as the theoretical values have been listed in Table 1. The theoretical densities of the composites were calculated by using reference data (the density of Al is 2.70 g cm^{-3}) based on the theoretical density of α-ZrW_2O_8 (ρ = 5.08 g cm^{-3}).[6] The measured density of all specimens exceeded 90% of the theoretical value, and that of the $ZrW_{2-x}Mo_xO_8$/Al (x = 0.0, 1.0) specimens were close to the estimated theoretical density. Furthermore, the relative density of the ceramic–metal composites was found to increase with the increase in metal content. The coefficients of thermal diffusion and the specific heat were measured by the conventional laser flash method using a thermal constant analyzer (ULVAC, TC7000, Kanagawa, Japan). The thermal conductivity coefficients were calculated from the experimental thermal diffusivity as well as the specific heat capacity and density values, which were measured by Archimedes' principle.

3. Results and discussion

3.1 Fabrication of $ZrW_{2-x}Mo_xO_8$/Al composites

Fig. 1 shows the *Z*-axis linear shrinkage curve of the Al 50 vol% ZrW_2O_8/Al composite at a sintering temperature of 873 K. In the temperature range of 300–370 K, a slight *Z*-axis shrinkage is observed, which may be due to the evaporation of H_2O and CO_3^{2-} on the surface of the pre-calcining powders. The remarkable shrinkage caused by the densification takes place at a temperature of 380 K and ends at a set temperature of 873 K. This indicates that Al and ZrW_2O_8 fuse with each other and reach densification in this temperature interval, and the SEM images of $ZrW_{2-x}Mo_xO_8$/Al composites shown in Fig. 3 can be observed in the mixed state of metal matrix and ceramic. The XRD patterns of ZrW_2O_8/Al and $ZrWMoO_8$/Al composites obtained after SPS sintering are shown in Fig. 2(a) and (b). All XRD patterns are similar, and the characteristic reflections of each phase were indexed to ZrW_2O_8 and Al. The absence of some special (221, 310) reflections for $x = 1.0$ samples is related to the occurrence of an order–disorder phase transformation, which shows variation in the space group from the low-temperature phase (space group: $P2_13$) to the high-temperature phase (space group: $Pa\bar{3}$). The fabrication stress during SPS and the thermal stress between ZrW_2O_8 and Al was not high enough to

Table 1 Density and relative density values of ZrW_2O_8/Al and $ZrWMoO_8$/Al composites

	ZrW_2O_8/Al			$ZrWMoO_8$/Al		
Al volume fraction (vol%)	Density (g cm^{-3})	Theoretical density (g cm^{-3})	Relative density (%)	Density (g cm^{-3})	Theoretical density (g cm^{-3})	Relative density (%)
0	4.80	5.08	94.5	4.17	4.33	96.3
30	4.10	4.37	93.8	3.56	3.84	92.7
50	3.91	3.89	101	3.33	3.52	93.9
70	3.35	3.41	98.2	2.93	3.19	91.9
100	2.69	2.70	99.8	2.69	2.70	99.8

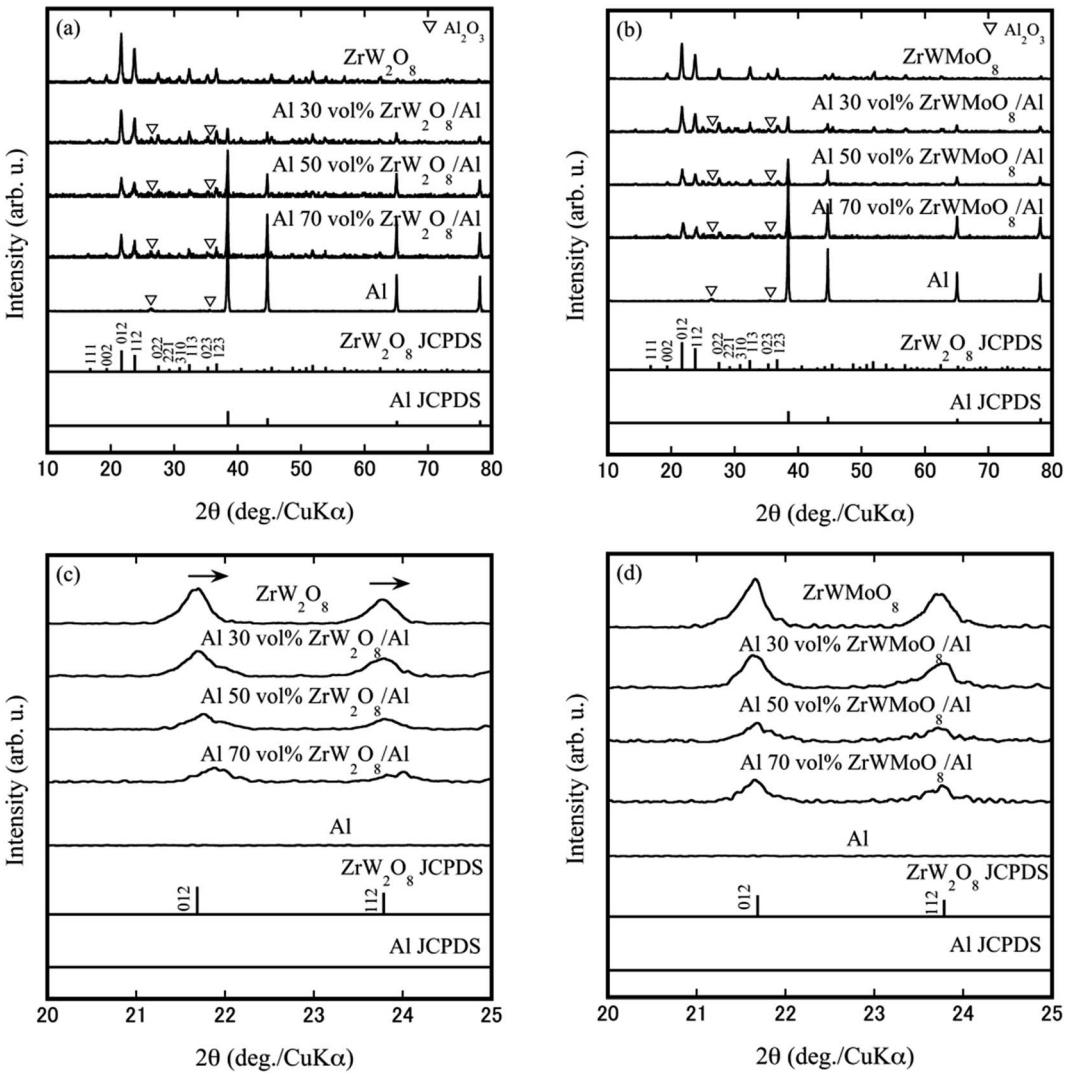

Fig. 2 XRD patterns of (a) and (c) ZrW_2O_8/Al composites and (b) and (d) $ZrWMoO_8$/Al composites.

be able to induce cubic–orthorhombic phase transition, which suggests the successful fabrication of ZrW_2O_8/Al composites without a high-pressure phase transition. However, some Al_2O_3 characteristic reflections were observed due to the partial oxidation of aluminum. Fig. 2(c) and (d) correspond to the (012) and (112) reflections in Fig. 2(a) and (b), respectively. No clear reflection shift was observed in the XRD patterns of the $ZrWMoO_8$/Al specimens, whereas the reflections of ZrW_2O_8/Al specimens shifted to higher angles as the Al volume fraction. In addition, the full width at half maximum (FWHM) of ZrW_2O_8/Al specimens increased upon increasing the Al volume fraction. This may be due to the fact that at lower sintering temperatures, $ZrWMoO_8$ has a relatively smaller compressive strain in the aluminum matrix than ZrW_2O_8 grains, and this difference in compressive strain will be reflected in the thermal expansion results below. The crystallite size corresponding to the FWHM of certain reflections (012, 112) using the Scherrer formula was calculated. The crystallite size range for the ZrW_2O_8/Al sample is between 120 nm and 180 nm, while for the $ZrWMoO_8$/Al sample, it falls between 170 nm and 270 nm. A comparison reveals that the crystallites in the ZrW_2O_8/Al specimens are finer than those in the $ZrWMoO_8$/Al specimens.

Fig. 3(a)–(f) shows the backscattered electron images of the microstructure of the polished surface of $ZrW_{2-x}Mo_xO_8$/Al (x = 0.0, 1.0). Different ceramic compositions resulted in different homogeneity of composites. Especially in the Al 70 vol% $ZrW_{2-x}Mo_xO_8$/Al composites, many 1 μm to 10 μm aggregates were observed in the ZrW_2O_8/Al specimen, whereas in the $ZrWMoO_8$/Al specimen, the aggregates had sizes from 100 nm to 1 μm, and the homogeneity of Al and $ZrWMoO_8$ was improved. The dispersed particles were smaller in the $ZrWMoO_8$/Al specimens, and there was less particle agglomeration. As a result, because the specific surface area of ZrW_2O_8 particles was larger than Al, the compressive stress generated from Al during cooling is expected to be larger than that in the $ZrWMoO_8$/Al specimens.

To better understand the dispersion of Al and ZrW_2O_8 particles and the composition of each component of the

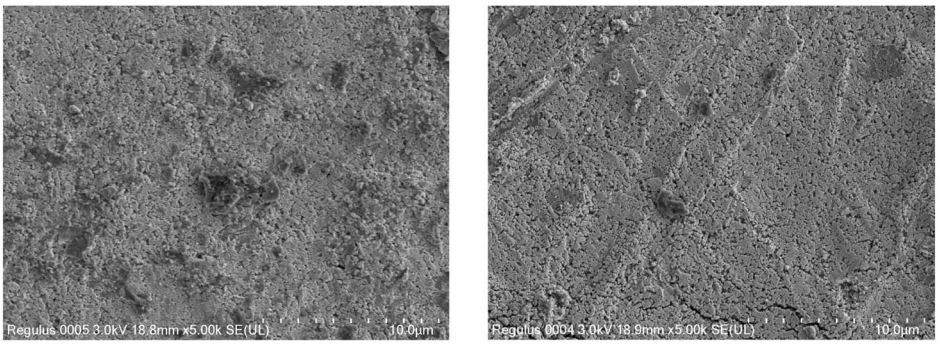

(a) Al 30 vol% ZrW_2O_8/Al

(b) Al 30 vol% $ZrWMoO_8$/Al

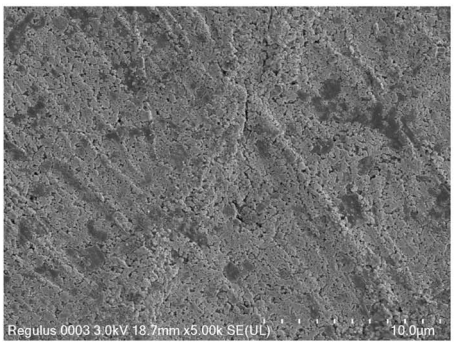

(c) Al 50 vol% ZrW_2O_8/Al

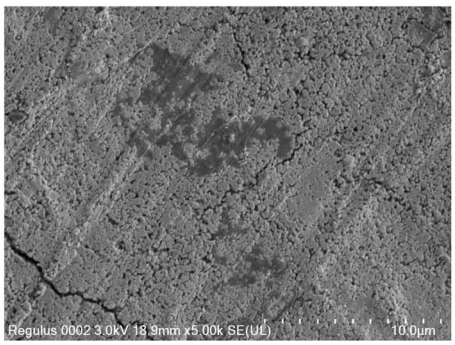

(d) Al 50 vol% $ZrWMoO_8$/Al

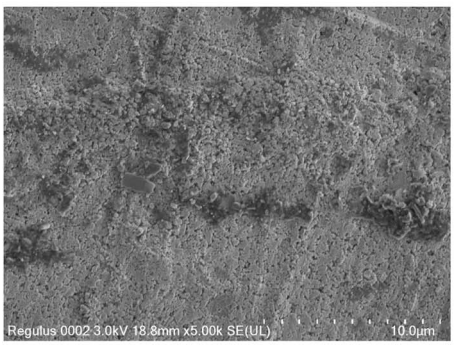

(e) Al 70 vol% ZrW_2O_8/Al

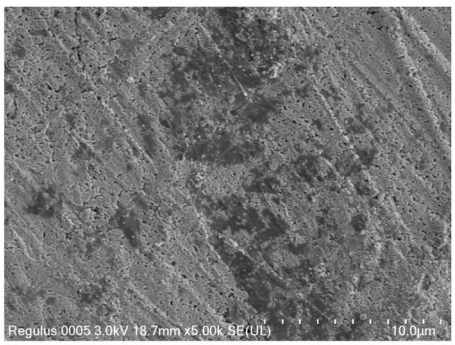

(f) Al 70 vol% $ZrWMoO_8$/Al

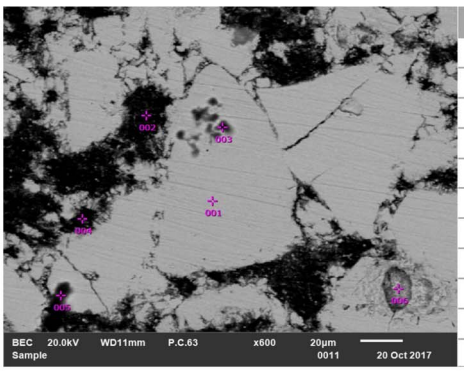

	1	2	3
molecular	atom%	atom%	atom%
O	66.83	9.53	71.53
Al	0.71	90.17	0.92
Zr	11.21	0.11	12.41
W	21.24	0.18	15.14
	4	5	6
molecular	atom%	atom%	atom%
O	18.92	62.63	32.47
Al	79.50	3.12	2.33
Zr	0.59	13.48	4.48
W	1.00	20.76	60.72

(g) SEM-EDX point analysis of the Al 30 vol% ZrW_2O_8/Al Al 30vol% ZrW_2O_8/Al

Fig. 3 (a–f) SEM images of the polished surface of $ZrW_{2-x}Mo_xO_8$/Al (x = 0.0, 1.0) composites; (g) SEM-EDX point analysis of the Al 30 vol% ZrW_2O_8/Al specimen.

composites, SEM-EDX point analysis was employed for investigating the elemental composition at six points of Al 30 vol% ZrW_2O_8/Al specimen (Fig. 3(g)). Point 1 seems to have ZrW_2O_8 as the main phase because the quantitative analysis shows that the ratio of Zr : W is about 1 : 2. Point 2 seems to have Al as the main phase, and the existence of oxygen may be related to the

oxidation of Al, but oxygen doesn't exist in a significant quantity. Al was highly oxidized at Point 4, which presumably lies near the tissue interface of Al and ZrW_2O_8. This is inevitable because the oxide-forming tendency of Al is low in comparison with other metals. The sparse black spots (Point 3 and Point 5) in the SEM image have a Zr : W ratio that deviates from 1 : 2. These spots may be due to impurities such as Al_2O_3 that were introduced as contaminants at the time of powder production. The same applies to Point 6.

3.2 Thermal expansion properties of $ZrW_{2-x}Mo_xO_8$/Al composites

The CTEs obtained from heating and cooling (three continuous repeat measurements) as a function of temperature are plotted in Fig. 4(a) and (b). For Al 50 vol% ZrW_2O_8/Al and Al 50 vol% $ZrWMoO_8$/Al specimens, the thermal expansion curves observed during the heating cycle increased continuously upon increasing the temperature and showed the same trend during the cooling cycle; however, it can be observed that the thermal expansion of the ZrW_2O_8/Al specimen during the first cycle was different from those observed during the second and third heating–cooling cycles, in which the sample could not shrink to its original length after one heating–cooling cycle. This may be related to the strain relaxation of ZrW_2O_8, in which the residual stresses resulted from the thermal mismatch between the matrix, and the ceramic distorted the sparse structure of ZrW_2O_8. Compared with the thermal expansion hysteresis behavior of ZrW_2O_8/Al composites, in the $ZrWMoO_8$/Al specimens, the thermal expansion was relatively consistent after the second heating and cooling cycle, indicating that the thermal deformation of the $ZrWMoO_8$/Al composites was small. Another clear difference between ZrW_2O_8 and $ZrWMoO_8$ is the presence or absence of a phase transition around 410–420 K, in which a change in the slope of the thermal expansion curve near the

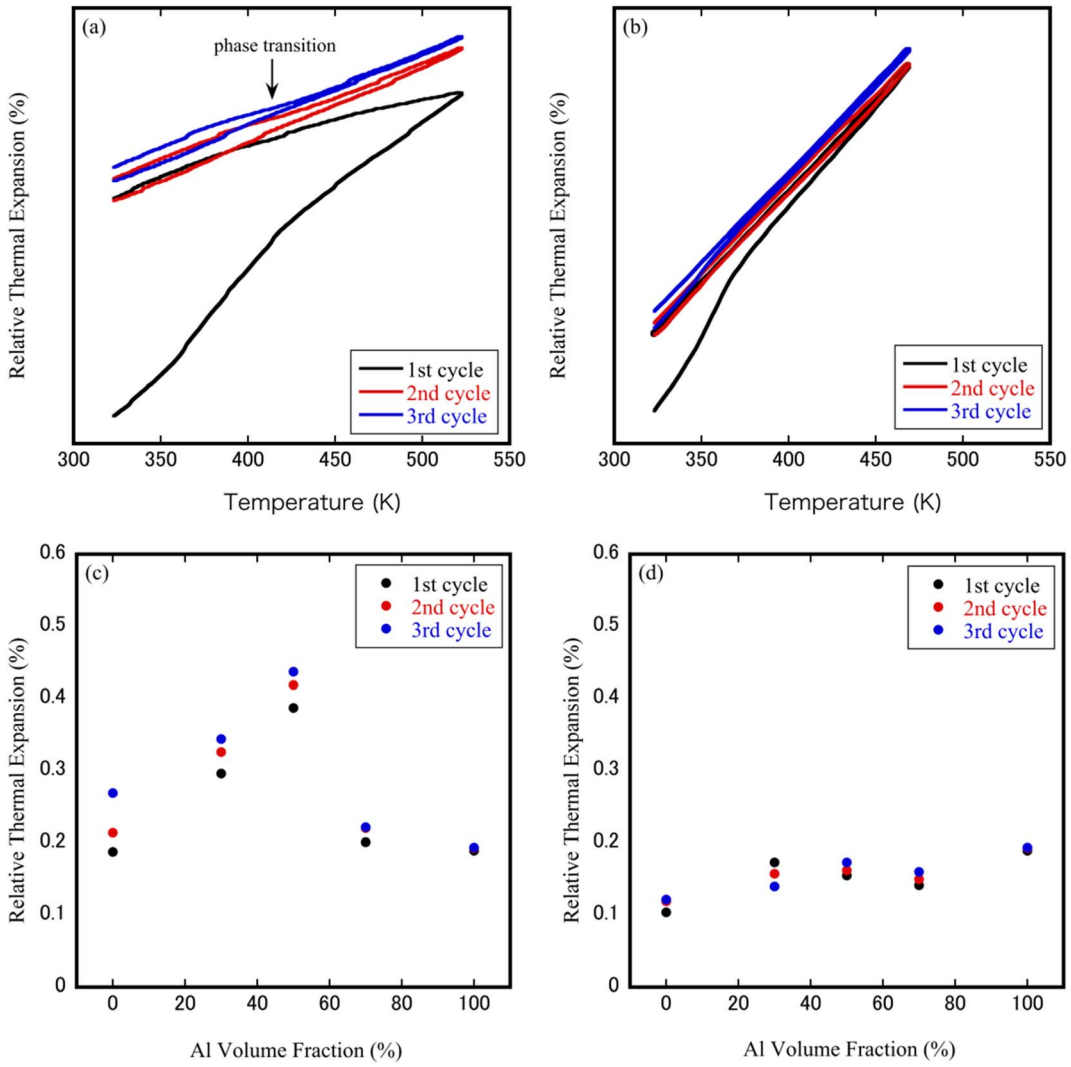

Fig. 4 TMA curves of (a) Al 50 vol% ZrW_2O_8/Al specimen and (b) Al 50 vol% $ZrWMoO_8$/Al specimen subjected to three heating–cooling cycles; change in the CTEs after heating cycle as a function of the volume fraction of (c) ZrW_2O_8/Al specimens and (d) $ZrWMoO_8$/Al specimens for three cycles.

phase transition temperature was observed in ZrW_2O_8/Al specimens. In contrast, the thermal expansion curves were straight lines for $ZrWMoO_8$/Al composites; therefore, it is suggested that a mismatched thermal expansion during the thermal cycles of ZrW_2O_8/Al may be affected by the particles dispersed in aluminum and also by phase transitions. This result verifies the XRD reflections shift in Fig. 2(c) and (d).

Fig. 4(c) and (d) depicts the changes in the CTEs after the heating cycle relative to the volume fraction of Al. In ZrW_2O_8/Al specimens, a convex parabolic trend can be observed, with the maximum CTE reached at 50 vol% Al. The change in the CTEs of ZrW_2O_8/Al specimens was about 0.1 to 0.3%, whereas the CTE variation of the $ZrWMoO_8$/Al sample remains more or less constant. This difference in CTE seems to be related to the dispersion state of $ZrW_{2-x}Mo_xO_8$ with Al. In the ZrW_2O_8/Al specimens, because the ZrW_2O_8 particles formed 100 μm agglomerates, the stress from Al relieved the agglomeration and pores of ZrW_2O_8. The ZrW_2O_8 particles subjected to stress from Al increased because the dispersed particle size was small in the $ZrWMoO_8$/Al specimens.

The thermal expansion behavior of the composites was further analyzed by comparing the experimental results with theoretical models. Several models have been proposed to estimate the CTEs of ceramic–metal composites.[30–32] Among them, the most widely used is the (ROM). ROM considers the matrix to be free of voids, in which each material is perfectly bonding to the matrix so that each component is distorted independently. CTEs are usually assumed to follow a linear ROM dependence on the volume fraction. Fig. 5(a) and (b) shows the thermal expansion of $ZrW_{2-x}Mo_xO_8$/Al ($x = 0.0$, 1.0) composites with different Al volume fractions obtained from the third heating cycle and a comparison with the values predicted by the ROM model. In contrast to the measured curves of $ZrWMoO_8$/Al composites were consistent with the theoretical curves of the ROM model, the measured curves of ZrW_2O_8/Al composites show a slight deviate from the theoretical curves of the ROM model, possibly due to the presence of nanoparticles, which led to residual stresses in the composites. Furthermore, the thermal expansion behavior of both composites confirmed that the CTEs changed from negative to near-zero to positive by

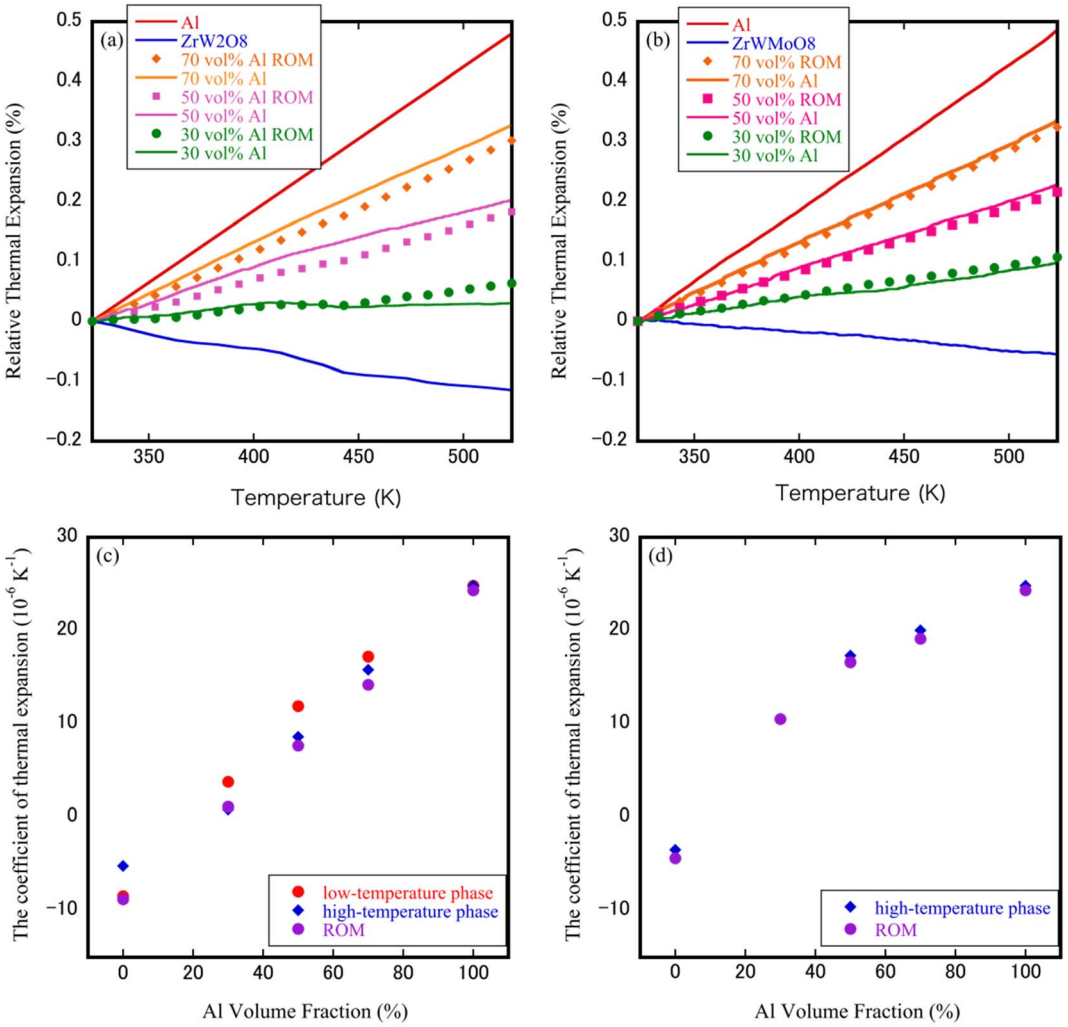

Fig. 5 TMA curves of (a) ZrW_2O_8/Al and (b) $ZrWMoO_8$/Al composites during the third heating cycle; CTEs of (c) ZrW_2O_8/Al and (d) $ZrWMoO_8$/Al composites.

changing the volume fraction of Al. For ZrW_2O_8/Al composites, mon-linear changes in the CTEs were observed around 420–440 K, which was associated with the order–disorder phase transition of α-ZrW_2O_8 to β-ZrW_2O_8.

The CTEs of $ZrW_{2-x}Mo_xO_8$/Al (x = 0.0, 1.0) composites measured by thermo-mechanical analysis and estimated based on the ROM model are plotted in Fig. 5(c) and (d). The measured coefficients have values similar to the values reported for ZrW_2O_8 powders in the literature (α-ZrW_2O_8: -8.8×10^{-6} K^{-1}; β-ZrW_2O_8: -4.9×10^{-6} K^{-1}). Compared with the ZrW_2O_8/Al composites, the $ZrWMoO_8$/Al composites had slightly higher CTEs because the absolute value of the negative CTEs value of $ZrWMoO_8$ is smaller than that of ZrW_2O_8. Additionally, when the Al content rises, the value of the CTEs of ZrW_2O_8/Al composites at the room temperature gradually increases, from -8.46×10^{-6} K^{-1} for ZrW_2O_8 to 3.37×10^{-6} K^{-1} for Al 30 vol% specimen, 11.90×10^{-6} K^{-1} for Al 50 vol% specimen and rised to 17.20×10^{-6} K^{-1} for Al 70 vol% specimen. The same phenomenon was observed in $ZrWMoO_8$/Al composites, where the CTEs increased from -3.49×10^{-6} K^{-1} for $ZrWMoO_8$ to 10.54×10^{-6} K^{-1} for Al 30 vol% specimen, 17.29×10^{-6} K^{-1} for Al 50 vol% specimen, and 20.00×10^{-6} K^{-1} for Al 70 vol% specimen. This indicates that $ZrW_{2-x}Mo_xO_8$/Al (x = 0.0, 1.0) composites with a tunable thermal expansion coefficient (negative, positive, or close to zero) could be produced by adjusting the volume fraction of Al. Thus, this result suggests that the CTEs can be controlled to some extent by using $ZrWMoO_8$ as an inhibitor, as in the case of ZrW_2O_8. The two NTE ceramic materials as inhibitors have their own characteristics in controlling the thermal expansion properties, among which ZrW_2O_8 has a larger NTE coefficient, which can maintain the original properties (such as electrical conductivity, thermal conductivity) of the composite matrix, to a greater extent while regulating the CTEs; on the other hand, the advantage of $ZrWMoO_8$ is that it does not have the phase transition from the low-temperature phase to the high-temperature phase above room temperature, which avoids the drastic change of the CTEs during phase transition.

3.3 Thermal conductivity and electrical conductivity of $ZrW_{2-x}Mo_xO_8$/Al composites

Fig. 6(a) and (b) shows the thermal conductivity and electrical conductivity coefficients of $ZrW_{2-x}Mo_xO_8$/Al (x = 0.0, 1.0) composites at room temperature. It can be observed that the thermal and electrical conductivity curves of the ZrW_2O_8/Al and $ZrWMoO_8$/Al composites are basically the same. Furthermore, the thermal and electrical conductivity coefficients also show irregular non-linear curves with the variation of Al volume fraction, unlike the linear proportionality observed in the CTEs result. To the best of our knowledge, the electrical conductivity of $ZrW_{2-x}Mo_xO_8$/Al composites is not inherently random; it is determined by the composition, arrangement, and interactions of the components. However, there can be some variability due to factors like the distribution and orientation of conductive particles, as well as the quality of the interface between the conductive (Al) and non-conductive ($ZrW_{2-x}Mo_xO_8$) phases. We believe that the close packing or dispersed arrangement of Al particles can influence the electron conduction within the composite material. Additionally, non-uniform distribution or different orientations of $ZrW_{2-x}Mo_xO_8$ (x = 0, 1) ceramic particles and Al particles can result in uneven electrical conductivity in the $ZrW_{2-x}Mo_xO_8$/Al composites. Fig. 7 presents a schematic simulation of the internal electron conduction in $ZrW_{2-x}Mo_xO_8$/Al composites with varying aluminum volume fractions. When the Al volume fraction is low (0–30vol%), the structure of $ZrW_{2-x}Mo_xO_8$/Al composites is such that Al is isolated and dispersed in $ZrW_{2-x}Mo_xO_8$, and the free electron conduction path to Al is blocked by the $ZrW_{2-x}Mo_xO_8$ insulator, resulting in limited connection and propagation of free electrons. In this case, the thermal conductivity is thought to be dominated by the phonon contributions of Al and $ZrW_{2-x}Mo_xO_8$, which contribute little to the thermal conductivity. As the Al volume fraction in the composite increases to 50 vol%, both phonons and electrons contribute to the rapid change in thermal conductivity, with the heat conduction shifting from phonon to

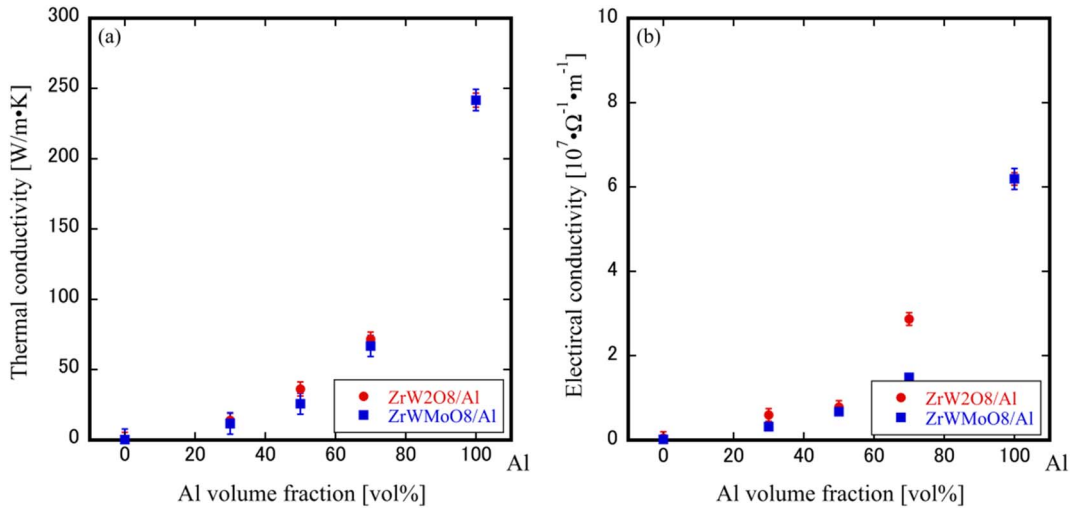

Fig. 6 (a) Thermal conductivity and (b) electrical conductivity of $ZrW_{2-x}Mo_xO_8$/Al composites at room temperature.

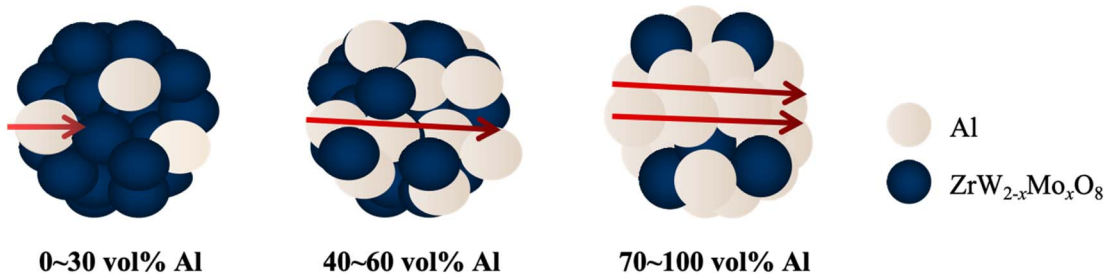

Fig. 7 Simulation diagram of internal electron conduction in ZrW_2O_8/Al composites with different Al volume fraction.

free electron contribution, and the electron conduction starting to proceed smoothly. The substantial increase in conductivity with the same Al volume fraction is more definitely attributed to the conduction path where the connection and propagation of free electrons occur. When the Al content is as high as 70 to 100 vol%, $ZrW_{2-x}Mo_xO_8$ is isolated and dispersed in Al, with the contribution of phonons to the thermal conductivity being minimal and the contribution of free electrons from Al being dominant in conduction. Therefore, when the Al content is high, the conduction paths of the electron conduction carriers are connected, and the propagation of the dominant conduction electrons is smooth, resulting in high values of thermal and electrical conductivity.

4. Conclusion

High-density cubic-phase $ZrW_{2-x}Mo_xO_8$/Al (x = 0.0, 1.0) composites were successfully fabricated by spark plasma sintering, and their microstructure, thermal expansion properties and thermal (electrical) conductivity were characterized and analyzed. The main conclusions are as follows: the ZrW_2O_8/Al and $ZrWMoO_8$/Al composites prepared at z-axis 90 MPa pressure and sintering temperatures of 873 K and 773 K, respectively, did not induce the formation of the high-pressure phase γ-$ZrW_{2-x}Mo_xO_8$. The thermomechanical analysis results showed that the volume fraction of Al particles significantly affected the thermal expansion of the composites. The CTEs of the $ZrW_{2-x}Mo_xO_8$/Al composites could be controlled from near-zero to positive simply by changing the volume fraction of Al, and the experimental CTEs had similar values to those predicted by the ROM models. Moreover, the thermal conductivity and electrical conductivity of the $ZrW_{2-x}Mo_xO_8$/Al composites can be increased with the increase of Al content in order to formulate reasonable coefficients of thermal expansion, thermal conductivity and electrical conductivity by setting the volume fraction of Al. It means that $ZrW_{2-x}Mo_xO_8$/Al composites have potential applications in electronic devices such as heat sinks that require thermal expansion regulation.

Conflicts of interest

The authors declare that there are no known competing financial interests or personal relationships which have appeared to affect the work reported herein.

Acknowledgements

This work was supported by National Natural Science Foundations of China (52302058); Key Projects of Natural Science Research in universities of Anhui Province (KJ2021A1023); Startup Research Fund of Chaohu University (KYQD-202010).

References

1 Y. Wu, M. Wang, Z. Chen, N. Ma and H. Wang, The effect of phase transformation on the thermal expansion property in Al/ZrW_2O_8 composites, *J. Mater. Sci.*, 2013, **48**, 2928–2933.
2 G. Wu, C. Zhou, Q. Zhang and R. Pei, Decomposition of ZrW_2O_8 in Al matrix and the influence of heat treatment on ZrW_2O_8/Al–Si thermal expansion, *Scr. Mater.*, 2015, **96**, 29–32.
3 N. Jing, S. Xu, Z. Wang and G. Wang, Enhanced Electrochemical Performance and Safety of Silicon by a Negative Thermal Expansion Material of ZrW_2O_8, *ACS Appl. Mater. Interfaces*, 2021, **13**, 30468–30478.
4 T. A. Mary, J. S. O. Evans, T. Vogt and A. W. Sleight, Negative thermal expansion from 0.3 to 1050 Kelvin in ZrW_2O_8, *Science*, 1996, **272**, 90–92.
5 A. W. Sleight, Compounds That Contract on Heating, *Inorg. Chem.*, 1998, **37**, 2854–2860.
6 J. S. O. Evans, T. A. Mary, T. Vogt, M. A. Subramanian and A. W. Sleight, Negative Thermal Expansion in ZrW_2O_8 and HfW_2O_8, *Chem. Mater.*, 1996, **8**, 2809–2823.
7 J. S. O. Evans, Negative thermal expansion materials, *Dalton Trans.*, 1999, **19**, 3317–3326.
8 J. S. O. Evans, W. I. F. David and A. W. Sleight, Structural investigation of the negative-thermal-expansion material ZrW_2O_8, *Acta Crystallogr., Sect. B: Struct. Sci.*, 1999, **55**, 333–340.
9 C. Closmann, A. W. Sleight and J. C. Haygarth, Low-Temperature Synthesis of ZrW_2O_8 and Mo-Substituted ZrW_2O_8, *J. Solid State Chem.*, 1998, **139**, 424–426.
10 J. S. O. Evans, P. A. Hanson, R. M. Ibberson, U. Kameswari, N. Duan and A. W. Sleight, Low-Temperature Oxygen Migration and Negative Thermal Expansion in $ZrW_{2-x}Mo_xO_8$, *J. Am. Chem. Soc.*, 2000, **122**, 8694–8699.
11 M. I. Ahmad, K. Lindley and M. Akinc, Hydrothermal Synthesis of $ZrW_{2-\delta}Mo_\delta O_8$ (δ=0–0.91) and its $\alpha \rightarrow \beta$ Transformation, *J. Am. Ceram. Soc.*, 2011, **94**, 2619–2624.

12 Y. f. Shi, X. Chen, J. Han, H. Ma, X. Li, X. Yang and X. Zhao, Phase transition behavior for $ZrW_{2-x}Mo_xO_8$ compositions at elevated temperatures, *J. Solid State Chem.*, 2009, **182**, 2030–2035.

13 R. Zhao, X. Yang, H. Wang, J. Han, H. Ma and X. Zhao, A novel route to synthesize cubic $ZrW_{2-x}Mo_xO_8$ (x=0-1.3) solid solutions and their negative thermal expansion properties, *J. Solid State Chem.*, 2007, **180**, 3160–3165.

14 J. D. Jorgensen, Z. Hu, S. Teslic, D. N. Argyriou, S. Short, J. S. O. Evans and A. W. Sleight, Pressure-induced cubic-to-orthorhombic phase transition in ZrW_2O_8, *Phys. Rev. B: Condens. Matter Mater. Phys.*, 1999, **59**, 215–225.

15 J. S. O. Evans, J. D. Jorgensen, S. Short, W. I. F. David, R. M. Ibberson and A. W. Sleight, Thermal expansion in the orthorhombic γ phase of ZrW_2O_8, *Phys. Rev. B: Condens. Matter Mater. Phys.*, 1999, **60**, 14643–14648.

16 J. S. O. Evans, Z. Hu, J. D. Jorgensen, D. N. Argyriou, S. Short and A. W. Sleight, Compressibility, Phase Transitions, and Oxygen Migration in Zirconium Tungstate, ZrW_2O_8, *Science*, 1997, **275**, 61–65.

17 C. Zhou, Q. Zhang, S. Liu, T. Zhou, J. R. Jokisaari and G. Wu, Microstructure and thermal expansion analysis of porous ZrW_2O_8/Al composite, *J. Alloys Compd.*, 2016, **670**, 182–187.

18 C. Zhou, Y. Zhou, Q. Zhang, Q. Meng, L. Zhang, E. Kobayashi and G. Wu, Near-zero thermal expansion of ZrW_2O_8/Al–Si composites with three dimensional interpenetrating network structure, *Composites, Part B*, 2021, **211**, 108678.

19 H. Holzer and D. C. Dunand, Phase Transformation and Thermal Expansion of Cu/ZrW_2O_8 Metal Matrix Composites, *J. Mater. Res.*, 1999, **14**, 780–789.

20 S. Yilmaz, Thermal mismatch stress development in Cu-ZrW_2O_8 composite investigated by synchrotron X-ray diffraction, *Compos. Sci. Technol.*, 2002, **62**, 1835–1839.

21 C. Verdon and D. C. Dunand, High-temperature reactivity in the ZrW_2O_8-Cu system, *Scr. Mater.*, 1997, **36**, 1075–1080.

22 X. Yan, X. Cheng, G. Xu, C. Wang, S. Sun and R. Riedel, Preparation and thermal properties of zirconium tungstate/copper composites, *Materialwiss. Werkstofftech.*, 2008, **39**, 649–653.

23 S. Yilmaz, Phase transformations in thermally in thermally-cycled Cu/ZrW_2O_8 composites investigated by X-ray diffraction, *J. Phys.: Condens. Matter*, 2002, **14**, 365–375.

24 C. Zhou, C. Liu, Y. Zhou, H. Zhang, H. Sun, C. Yu, P. Song, Q. Zhang and G. Wu, Superior overall performance of zero thermal expansion ZrW_2O_8/Al–Si composite, *Ceram. Int.*, 2023, **49**, 34074–34082.

25 L. L. Y. Chang, M. G. Scroger and B. Phillips, Condensed Phase Relation in the Systems ZrO_2-WO_2-WO_3 and HfO_2-WO_2-WO_3, *J. Am. Chem. Soc.*, 1967, **50**, 211–215.

26 K. Kanamori, T. Kineri, R. Fukuda, K. Nishio, M. Hashimoto and H. Mae, Spark Plasma Sintering of Sol-Gel Derived Amorphous ZrW_2O_8 Nanopowder, *J. Am. Chem. Soc.*, 2009, **92**, 32–35.

27 K. Kanamori, T. Kineri, R. Fukuda, T. Kawano and K. Nishio, Low-temperature sintering of ZrW_2O_8-SiO_2 by spark plasma sintering, *J. Mater. Sci.*, 2009, **44**, 855–860.

28 H. Wei, J. Mei, Y. Xu, X. Zhang, J. Li, X. Xu, Y. Zhang, X. Wang and M. Li, Low-Temperature Rapid Sintering of Dense Cubic Phase $ZrW_{2-x}Mo_xO_8$ Ceramics by Spark Plasma Sintering and Evaluation of Its Thermal Properties, *Materials*, 2022, **15**, 4650.

29 H. Wei, J. Li, F. Hu, Y. Han, B. Chen, H. Li, Y. Zhang, X. Wang and X. Xu, Structural, In-situ Raman Spectroscopy and XPS Studies on $ZrW_{2-x}Mo_xO_8$ Ceramics with Tunable Negative Thermal Expansion Properties, *Ceram. Int.*, 2023, **49**, 28313–28325.

30 C. Ye, B. Shentu and Z. Weng, Thermal conductivity of high density polyethylene filled with graphite, *J. Appl. Polym. Sci.*, 2006, **101**, 3806–3810.

31 B. Lonnberg, Thermal Expansion Studies on the Group IV-VII Transition Metal Diborides, *J. Less-Common Met.*, 1988, **141**, 145–156.

32 E. S. Lee, S. M. Lee, D. J. Shanefield and W. R. Cannon, Enhanced thermal conductivity of polymer matrix composite via high solids loading of aluminum nitride in epoxy resin, *J. Am. Chem. Soc.*, 2008, **91**, 1169–1174.